Collective and noncollective states in ^{66}Zn

Indu Bala,[1,*] S. C. Pancholi,[1] M. K. Raju,[2] A. Dhal,[3] S. Saha,[4] J. Sethi,[4] T. Trivedi,[5] R. Raut,[6] S. S. Ghugre,[6] R. Palit,[4] R. P. Singh,[1] and S. Muralithar[1]

[1]*Inter-University Accelerator Centre, Aruna Asaf Ali Marg, New Delhi 110067, India*
[2]*Nuclear Physics Department, Andhra University, Visakhapatnam 530003, India*
[3]*Variable Energy Cyclotron Centre, Kolkata 700064, India*
[4]*Tata Institute of Fundamental Research, Mumbai 400005, India*
[5]*Guru Ghasidas Vishwavidyalaya, Bilaspur 495009, India*
[6]*UGC-DAE Consortium for Scientific Research, Kolkata Centre, Kolkata 700098, India*

(Received 26 October 2020; revised 11 July 2021; accepted 7 September 2021; published 4 October 2021)

Excited states in the ^{66}Zn nucleus were populated via a ^{56}Fe(^{12}C, $2p\gamma$) fusion-evaporation reaction at a beam energy of ≈62 MeV. The deexciting γ rays were detected using the Indian National Gamma Array (INGA). The level scheme of the ^{66}Zn nucleus has been updated by placing several new γ rays as well as by assigning the spin and parity of various excited states from the present spectroscopic results. The microscopic structure of the observed states have been investigated in the light of large shell-model calculations. The shape of this nucleus in the low-spin regime has been studied under the framework of total Routhian surface (TRS) calculations. The lifetime of first 3^- state at 2826 keV is experimentally measured using the Doppler-shift attenuation method and the deduced $B(E1)$ value indicates the presence of octupole collectivity in this nucleus.

DOI: 10.1103/PhysRevC.104.044302

I. INTRODUCTION

In-beam γ-ray studies of nuclei in the $A \approx 60$–80 mass region populated via heavy-ion-induced nuclear reactions have revealed a variety of physical phenomenon in these nuclei, which so far cannot be explained in the framework of a single theoretical model. Doubly magic ^{56}Ni is a spherical nucleus, and the deformation increases upon adding proton and/or neutron pairs to it. Also, the spectra of the deformed nuclei changes from the collective vibrational to the collective rotational as one goes from less-deformed Zn isotopes to more-deformed Se and Kr nuclei in the mass $A \approx 70$ region. Furthermore, the structure of these nuclei in mass $A \approx 60$–80 is reproducible neither with a harmonic vibrator nor with a pure symmetric rotor due to the presence of anharmonicities such as triaxial shapes and shape coexistence. Also, it is not possible to disentangle these different anharmonicities solely on the basis of the yrast level energies, but the physical interpretation of sidebands is also needed to fully describe these transitional nuclei. Thus, this mass region is a good testing ground for the development of theoretical models to explain the observed spectra.

The nucleon orbital configuration of the bandheads of yrast and yrare bands strongly depends on the orbitals present near the Fermi surface of the nuclei. The presence of intruder high-angular-momentum orbitals near the Fermi surface drives the nucleus towards deformation. In the mass region of $A \approx 60$–80 one expects that $\nu g_{9/2}$ and $\pi g_{9/2}$ orbitals play a significant role in deciding the structure and shape of the nuclei when excited in low and high-angular-momentum states. Furthermore, the study of shapes in mass region ($A \approx 60$–80) is of current interest as shape isomerism and triaxial shapes have been reported by different groups [1,2]. For example, recently, the ^{66}Ni nucleus has been claimed of having three different shapes showing the shape isomerism at low spins [1], and the ^{64}Zn nucleus is supposed to have $E(5)$ symmetry at low spins [2], which motivates us to look into the structure of the nearby ^{66}Zn nucleus. Furthermore, the presence of the negative-parity states close to the positive-parity ground state in even-even Zn nuclei encourages us to explore the presence of octupole collectivity. The regions of nuclei with the strong octupole correlations correspond to the particle numbers near 34 ($g_{9/2} \leftrightarrow p_{3/2}$ coupling), 56 ($h_{11/2} \leftrightarrow d_{5/2}$ coupling), 88 ($i_{13/2} \leftrightarrow f_{7/2}$ coupling), and 134 ($j_{15/2} \leftrightarrow g_{9/2}$ coupling) [3–5]. Hence, it is quite possible that the octupole correlations are playing an important role in structure and shape of ^{66}Zn ($Z = 30$, $N = 36$) nucleus in which $\nu g_{9/2}$ and $\nu p_{3/2}$ orbitals are present near the Fermi surface.

The primary aim of the present investigation is to provide additional information on excited states of the ^{66}Zn nucleus and to understand its microscopic and macroscopic structure. Previous work on the structure of the ^{66}Zn nucleus is done mostly using light-ion beams, i.e., α and p with modest detector setups [6–14]. Recently, the high-spin states of the ^{66}Zn nucleus has been studied by Rai *et al.* [15] via heavy-ion nuclear reaction, where the level scheme is extended in the high-spin region, and Routhian surface calculations have been done for the low- as well as for the high-spin states of both positive- and negative-parity yrast bands.

*indu.phy@gmail.com; indu@iuac.res.in

 ©2021 American Physical Society

In the present work, the level scheme has been confirmed and extended, both for the low- as well as the high-spin states, and many new states have been observed based on non-yrast bandheads. The experimental results obtained for the high-spin states are compared with the shell-model calculations to have a microscopic view of the nucleus. To understand the nucleus macroscopically, Ttotal Routhian surface (TRS) calculations have been carried out. Furthermore, the upper limit of the lifetime of the 3^- state is measured using the Doppler-shift attenuation method (DSAM).

The present paper is organized as follows: details of the experimental setup and data analysis are given in Sec. II, Sec. III deals with the experimental results and their interpretation, and finally the summary of the present study is given in Sec. IV.

II. EXPERIMENTAL DETAILS, METHODOLOGY, AND DATA ANALYSIS

The high-spin states in the ^{66}Zn nucleus were populated via ^{56}Fe(^{12}C, $2p\gamma$) fusion-evaporation reaction at a beam energy of ≈62 MeV, delivered from the 14UD pelletron accelerator facility at Tata Institute of Fundamental Research (TIFR), Mumbai, India. Fifteen Compton-suppressed clover HPGe detectors of the Indian National Gamma Array (INGA) were employed to detect the deexciting γ rays [16,17]. The clover detectors were arranged at six different angles, *viz.*, two each at $\theta = 40^\circ,\ 65^\circ,\ 115^\circ,\ 140^\circ$, three at $\theta = 157^\circ$, and four at $\theta = 90^\circ$ with respect to the beam direction. About 5×10^9 twofold or higher-fold γ events were recorded via a fast digital data-acquisition system based on Pixie-16 modules made by XIA LLC [17,18]. The energy and efficiency calibrations of the detectors were carried out using radioactive ^{152}Eu and ^{133}Ba sources. The time-stamped gain-matched raw data were sorted into different 4 k × 4 k symmetric and asymmetric matrices with a 100 ns coincidence time window using the multiparameter time-stamped based coincidence search program (MARCOS), developed at TIFR [17]. Offline data analysis was carried out using the RADWARE [19,20] and CANDLE [21] analysis packages.

The level scheme of the ^{66}Zn nucleus has been updated by placing the newly observed γ rays on the basis of γ-γ coincidence and intensity relationships. The multipolarities of the observed γ transitions have been determined from the results of angular correlation ($R_{\rm DCO}$), as prescribed in Refs. [22,23]. To find the directional correlation from the oriented state ratio ($R_{\rm DCO}$), angle-dependent matrices were formed with events recorded at 90° (θ_2) along one axis and those at 157° (θ_1) along the other. $R_{\rm DCO}$ is defined as

$$R_{\rm DCO} = \frac{I_{\gamma_1}^{\theta_1}(\text{gated by } \gamma_2 \text{ at } \theta_2)}{I_{\gamma_1}^{\theta_2}(\text{gated by } \gamma_2 \text{ at } \theta_1)}, \tag{1}$$

where $I_{\gamma_1}^{\theta_1}$ ($I_{\gamma_1}^{\theta_2}$) is the intensity of γ_1 at the angle θ_1 (θ_2) when the energy gate is set on γ_2 at the angle θ_2 (θ_1). In the present investigation, the detectors at $\theta_1 = 157^\circ$ and $\theta_2 = 90^\circ$ with respect to the beam direction were used to evaluate the $R_{\rm DCO}$ values for multipolarity assignment of the γ-ray transitions. If the gating transition is of stretched quadrupole multipolarity then this ratio ≈1 for the stretched-quadrupole transitions and ≈0.5 for the stretched-dipole transitions. However, this ratio ≈2 for the stretched-quadrupole transitions and ≈1 for stretched dipoles if the gating transition is of the stretched-dipole multipolarity. For mixed dipole-quadrupole transitions, $R_{\rm DCO}$ depends on the mixing ratio.

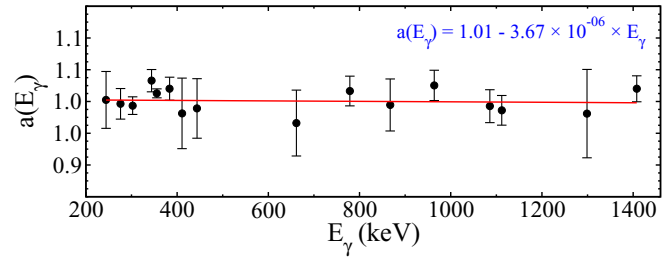

FIG. 1. Asymmetry factor "*a*" vs γ-ray energy for a 90° clover detector in the present setup. Solid red line shows linear fit to the data.

Furthermore, the advent of the CLOVER detector arrays (e.g., INGA) facilitated the determination of the electromagnetic character of the γ rays because the Clover detectors behave as a Compton polarimeter [24]. The integrated polarization directional correlation from oriented nuclei (IPDCO) method [24,25] has been used to determine the electromagnetic nature of the observed γ transitions. Clover detectors positioned at 90° with respect to the beam axis are most sensitive to this kind of measurement. For a linearly polarized photon scattered from a free electron at rest, the differential cross-section is given by the Klein–Nishina formula [26]. For this measurement, two asymmetric E_γ-E_γ matrices were constructed with horizontally or vertically scattered γ rays at 90° detectors on one axis and the coincident γ-ray events from all other detectors on the second axis. The number of parallel ($N_\parallel$) and perpendicular ($N_\perp$) scattered events for a given γ ray were obtained from the projection spectra by gating on the particular transitions of the ^{66}Zn nucleus. The linear polarization asymmetry ratio can be expressed as

$$\Delta(E_\gamma) = \frac{a(E_\gamma)N_\perp - N_\parallel}{a(E_\gamma)N_\perp + N_\parallel}. \tag{2}$$

Here, the asymmetry correction factor

$$a(E_\gamma) = N_\parallel(\text{unpolarized})/N_\perp(\text{unpolarized}) \tag{3}$$

represents the geometrical (instrumental) asymmetry of the detection system (INGA). It was determined by using the unpolarized radioactive ^{152}Eu and ^{133}Ba γ sources and its value found to be close to unity [1.01(0.01)] (see Fig. 1) for the present experimental setup. If the linear polarization asymmetry ratio [Eq. (2)] comes out to be positive then the γ-ray transition is *electric* in nature and if this comes out to be negative then the transition is said to be *magnetic* in nature. Based on the above methods, the results obtained from the present experiment and their interpretation are discussed in the next section.

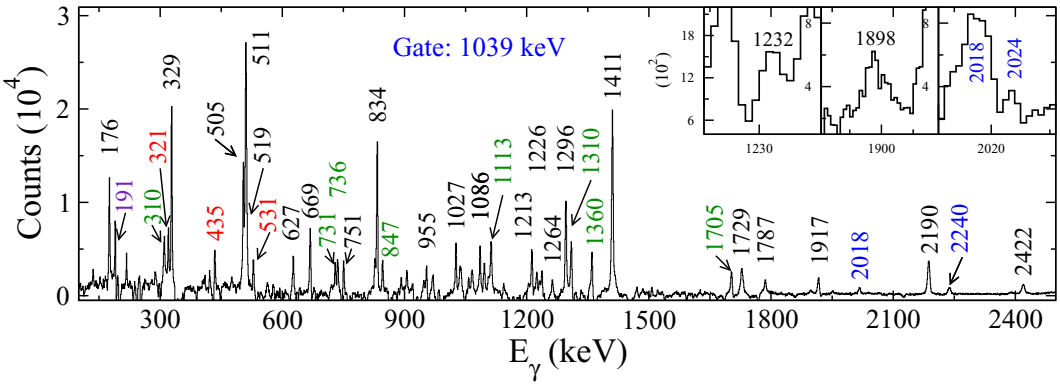

FIG. 2. The projected spectrum of E_γ-E_γ matrix gated by the 1039 keV $2^+ \rightarrow 0^+$ transitions. Known transitions belonging to ^{66}Zn nucleus are labeled with respective energies using black and the newly observed transitions are indicated by blue, the indigo peak is from ^{65}Ga, the green peaks are from ^{61}Cu, while the peaks which could not be identified or placed in the level scheme are shown in red.

III. EXPERIMENTAL RESULTS AND INTERPRETATIONS

The level scheme of the ^{66}Zn nucleus, populated via the ^{56}Fe(^{12}C, $2p$) ^{66}Zn reaction, is constructed on the basis of γ-γ coincidence relationships and intensity considerations. Based on the analysis and gating conditions, the gated spectra are generated, and a few for representation are shown in Figs. 2–4. The obtained level scheme, based on the above considerations, consisting of both positive- and negative-parity states, is shown in Fig. 5.

Seventeen new γ transitions and four tentative transitions (in red, see Fig. 5) are identified and placed in the level scheme. The ground-state yrast band is populated up to 15^+ spin at 9823 keV, confirming the results of a recent paper [15]. Other non-yrast bands of low intensity are added to the level scheme in the present work. Figure 2 shows the spectrum after gating on the 1039 keV transition ($2^+ \rightarrow 0^+$) on one of the axes of the symmetric E_γ-E_γ matrix. The blue colored transitions, viz., 2018, 2024, and 2240 keV transitions are the newly observed transitions along with the other known transitions. Further, Fig. 3 shows spectra obtained after gating the different γ-ray transitions written on the upper-right side of each panel and the new γ-ray transitions obtained in these gated spectra are placed in the level scheme. Furthermore, Fig. 4 shows the projected spectra of the E_γ-E_γ-E_γ cube obtained after gating on two of its axes; the gated transitions are shown in the upper-right side of the spectra shown. The γ transitions 2422, 1917, 1508, 1356, 1232, and 1418 keV are clearly visible now but were less prominent in the projected spectra of the E_γ-E_γ matrix by single gating condition. The relative γ-ray intensities have been normalized with respect to the 1039 keV transition ($2^+ \rightarrow 0^+$) intensity. The γ-ray transition energies, their relative intensities, $R_{\rm DCO}$, and the linear polarization asymmetry values obtained from the present work, are listed in Table I. Furthermore, the level scheme is discussed below.

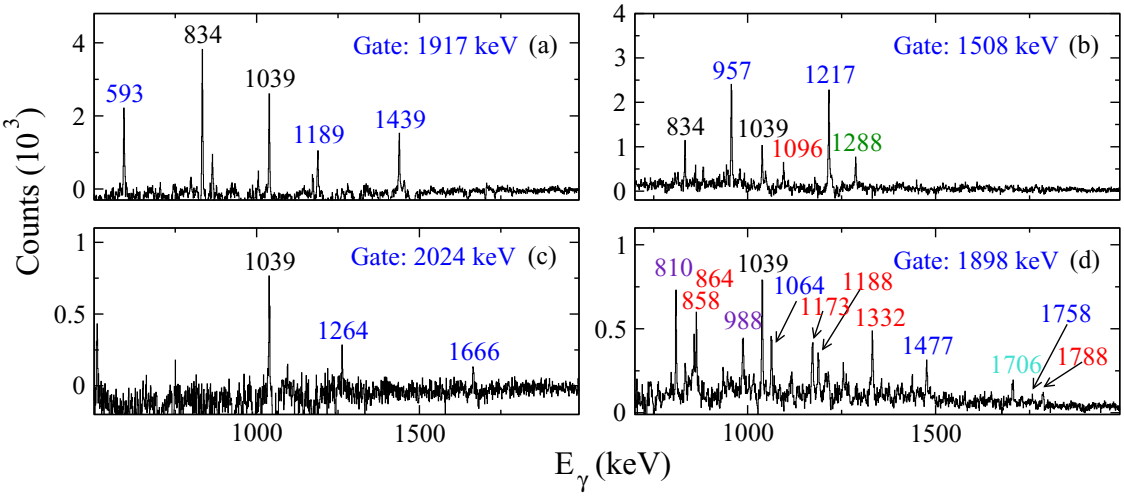

FIG. 3. Spectra of prompt γ rays observed in coincidence with the (a) 1917, (b) 1508, (c) 2024, and (d) 1898 keV γ rays belonging to ^{66}Zn. Newly observed transitions are indicated by the blue color. The green γ ray [in panel (b)] is from the other channel ^{66}Ge populated in this experiment. The indigo γ rays [in panel (d)] are from ^{63}Zn, the turquoise γ rays are from ^{51}Co, and the red γ rays [in panels (b) and (d)] are unknown and could not be placed in the level scheme.

TABLE I. The details of γ ray transitions of the ^{66}Zn nucleus observed in the present work.

E_i (keV)	E_γ (keV)[a]	I_γ(rel.)[b]	R_{DCO}	Δ_{Pol}	$J_i^\pi \rightarrow J_f^\pi$
1039	1039.4	100(2)	1.04(0)	0.11(1)	$2^+ \rightarrow 0^+$
1873	833.7	19.79(75)	0.94(3)[c]	0.04(1)	$2^+ \rightarrow 2^+$
2372	1333.2				$0^+ \rightarrow 2^+$
2450	1410.8	42.80(83)	0.86(5)[c]	0.08(1)	$4^+ \rightarrow 2^+$
2765	892.4	2.68(92)	1.55(14)[c]		$4^+ \rightarrow 2^+$
2826	1786.6	6.73(72)	0.59(6)[c]	0.02(3)	$3^- \rightarrow 2^+$
2937	1898.1	2.10(70)	0.92(12)[c]		$2^+ \rightarrow 2^+$
3057	2017.8	2.37(70)	1.09(13)[c]	−0.05(4)	$1^+ \rightarrow 2^+$
3063	2024.3				$(2^+) \rightarrow 2^+$
3077	1204.4				
	627.4	5.13(71)			
3105	1232.3	3.29(70)	0.97(9)[d]		$0^+ \rightarrow 2^+$
3229	2189.5	15.69(90)	0.98(4)[c]	−0.02(2)	$1^+ \rightarrow 2^+$
	1356.4		0.92(40)[d]		$1^+ \rightarrow 2^+$
	856.7				$1^+ \rightarrow 0^+$
3279	2239.8	3.92(71)	0.99(12)[c]		$4^{(+)} \rightarrow 2^+$
3381	2341.5				$1^- \rightarrow 2^+$
	1507.7	0.95(70)			$1^- \rightarrow 2^+$
	1008.6				$1^- \rightarrow 0^+$
3577	1704.1		0.75(7)[d]	−0.03(3)	$4^+ \rightarrow 2^+$
	751.2	4.00(70)			$4^+ \rightarrow 3^-$
3746	1296.4	18.40(76)	0.50(2)[c]	0.08(2)	$5^- \rightarrow 4^+$
	981.4				$5^- \rightarrow 4^+$
	920.0	1.55(70)			$5^- \rightarrow 3^-$
	669.0	7.97(72)	0.67(14)[c]	0.07(2)	$5^- \rightarrow 4^+$
3790	2751		0.95(2)[c]		$1^+ \rightarrow 2^+$
	1917.0	5.81(72)	1.08(10)[d]	0.10(4)	$1^+ \rightarrow 2^+$
	1418.2				$1^+ \rightarrow 0^+$
	685.5				$1^+ \rightarrow 0^+$
4001	1064.1				$(4^+) \rightarrow 2^+$
4075	328.6	13.46(74)	0.80(2)[c]	−0.07(3)	$6^- \rightarrow 5^-$
4179	1728.9	11.33(76)	1.10(5)[c]	0.09(3)	$6^+ \rightarrow 4^+$
4251	504.8	13.25(74)	1.06(3)[c]	0.06(2)	$7^- \rightarrow 5^-$
	175.9	5.28(71)	0.86(3)[c]		$7^- \rightarrow 6^-$
4279	1173.8				$(2^+) \rightarrow 0^+$
4295	2421.6	6.31(72)	1.13(11)[c]	−0.03(3)	$1^+ \rightarrow 2^+$
	1189.9				$1^+ \rightarrow 0^+$
	1066.0		0.61(3)[d]		$1^+ \rightarrow 1^+$
4327	1263.8				$(4^+) \rightarrow (2^+)$
4338	957.4				$(3^-) \rightarrow 1^-$
	1888.3				$(3^-) \rightarrow 4^+$
5206	1026.7	6.97(73)	1.10(7)[c]	0.11(3)	$8^+ \rightarrow 6^+$
	954.6	4.81(82)	0.60(4)[c]	0.00 (3)	$8^+ \rightarrow 7^-$
5229	1438.8				
5464	1213	8.41(73)		0.12(3)	$9^- \rightarrow 7^-$
5478	1477.1				$(6^+) \rightarrow (4^+)$
5555	1217.2				$(5^-) \rightarrow (3^-)$
	1376.3				$(5^-) \rightarrow 6^+$
5806	1526.9				$(4^+) \rightarrow (2^+)$
5822	593.3				
5993	1666.2				$(6^+) \rightarrow (4^+)$
6292	1085.8	6.78(73)	1.03(4)[c]	0.12(3)	$10^+ \rightarrow 8^+$
	828.2	4.23(71)	1.57(7)[c]	0.08(3)	$10^+ \rightarrow 9^-$
6418	1188.7				
7009	1454.1				$(7^-) \rightarrow (5^-)$
7236	1757.9				$(8^+) \rightarrow (6^+)$
7518	1225.6	3.70(72)	0.95(8)[c]	0.02(3)	$12^+ \rightarrow 10^+$

TABLE I. (*Continued.*)

E_i (keV)	E_γ (keV)[a]	I_γ(rel.)[b]	R_{DCO}	Δ_{Pol}	$J_i^\pi \rightarrow J_f^\pi$
7537	1731.2				$(6^+) \rightarrow (4^+)$
7955	1961.8				
7928	1935.2				
9304	1786.1				$(14^+) \rightarrow 12^+$
9823	519.2				$(15^+) \rightarrow (14^+)$

[a]The uncertainties lie between 0.1 to 0.5 keV depending upon the intensities.
[b]When intensity is not provided, it is due to low statistics and/or presence of a high-intensity neighboring γ ray.
[c]From the quadrupole gate at 1039 keV.
[d] From the quadrupole gate at 834 keV.

A. Positive- and negative-parity bands

Band 1. The yrast positive-parity band is studied by Cleeman *et al.* [6] and its extension by Rai *et al.* [15] is well reproduced and confirmed up to (15^+) at 9823 keV in the present experimental study.

Structure 2. The 1^+ state at 3790 keV had been observed in the earlier studies in the scattering experiments, viz., the (p, p') reaction. We have observed the 1917 keV γ ray in coincidence with 834 and 1039 keV [see Fig. 4(a)] and the 2751 keV γ ray in coincidence with 1039 keV, thus confirming the observation of the 3790 keV level. Furthermore, three new transitions at 1439, 1189, and 593 keV have been observed in coincidence with the 1917, 834, and 1039 keV transitions [see Fig. 3(a)], and they are placed in the level scheme according to their intensity and coincidence relationships, decaying from the 5229, 6418, and 5822 keV levels.

Band 3. An earlier known level at 3105 keV, 0^+, is also observed in the present study. We were able to build a band on this level by placing two new transitions, 1174 and 1527 keV, and one tentative transition of 1731 keV above. All these are observed in coincidence with 1232, 834, and 1039 keV transitions.

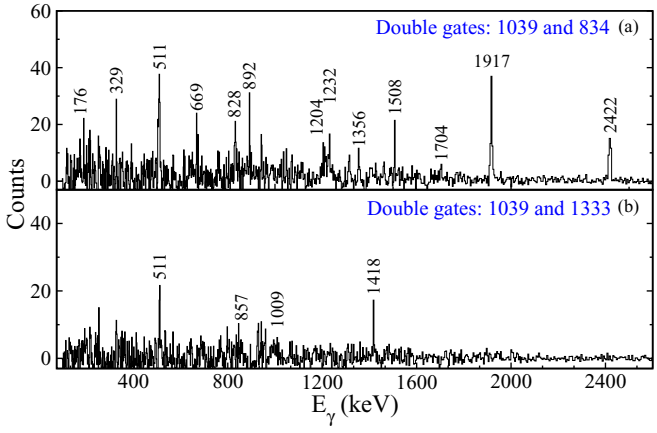

FIG. 4. The one-dimensional projection spectra of the E_γ-E_γ-E_γ cube gated by (a) 1039 keV on one axis and 834 keV on the other axis, (b) 1039 keV on one axis and 1333 keV on the other axis. The γ lines of 2422, 1917, 1508, 1356, 1232, and 1418 keV are clearly visible now.

Band 4. This band is established on the 2^+ level at 2937 keV. In our data we observed a 1898 keV transition in coincidence with 1039 keV [see Fig. 2 (inset)]. Further analysis enables us to observe 1064 and 1477 keV transitions, all in coincidence with each other [see Fig. 3(d)]. Based on these observations, two new levels have been put in the level scheme at 4001 and 5478 keV. One tentative γ ray and corresponding level is also given in the level scheme at 7236 keV.

Band 5. The newly observed γ transitions at 2018, 2024, and 2240 keV are found in coincidence with the 1039 keV transition [see Figs. 2 and 4(a)]. Also, the 1264, 1666, 1962, and 1935 keV transitions are found in coincidence with the 2024 and 1039 keV transitions. These are added to the level scheme in band 5 according to their coincidence relations. A tentative spin and parity has also been assigned to the band levels.

Band 6. The 3381 keV level 1^- has been observed in the present data with the observation of 2342, 1508, and 1009 keV γ transitions in coincidence with 1039, 834, and 1333 keV γ transitions, respectively. A new band has been identified with the addition of 957 and 1217 keV γ rays above the known level at 3381 keV [see Fig. 3(b)]. Furthermore, an interconnecting transition of 1888 keV from band 5 (3^-) to band 1 (4^+) is observed. One tentative transition of 1454 keV above and one interconnecting transition of 1376 keV is also added to this band.

Furthermore, the experimental lifetime measurement and its usage to describe the nuclear properties are discussed in the next section.

B. Lifetime measurement

Doppler shapes have been observed for the 1787 keV γ transition deexciting from 2826 keV, the 3^- state, and these were analyzed to determine the corresponding level lifetime. The developments reported by Das *et al.* [27] along with the LINESHAPE [28,29] package were used for this purpose. The application of the former facilitated the incorporation of the updated and experimentally validated stopping powers from the SRIM [30] database as well as of the evolving cross section of the ^{66}Zn residue, with changing beam energy, along the depth of the thick target. As per the standard procedure of the DSAM, the level lifetime was determined by least square fitting of the calculated Doppler shapes to the experimental spectra at four different angles, namely, 157°, 140°, 115°, and

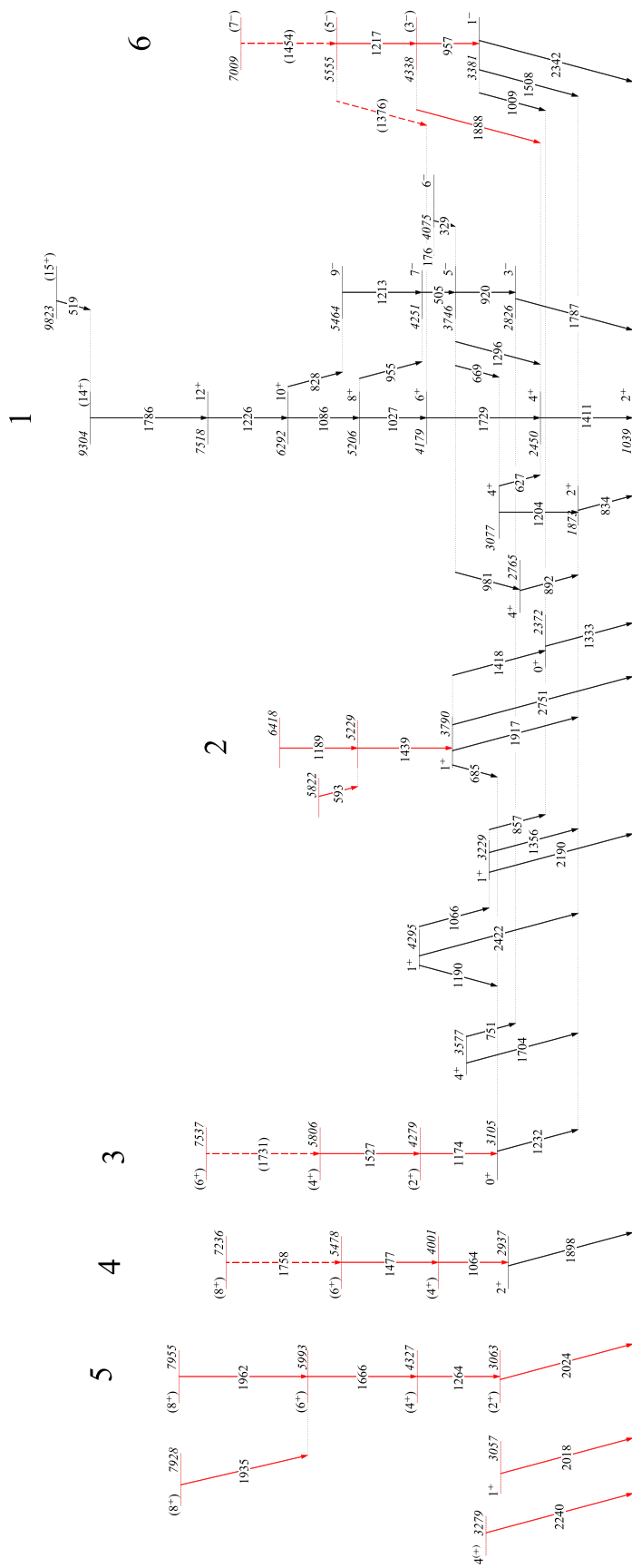

FIG. 5. Level scheme of ^{66}Zn nucleus deduced from this work. Newly observed γ transitions and energy levels are shown in red.

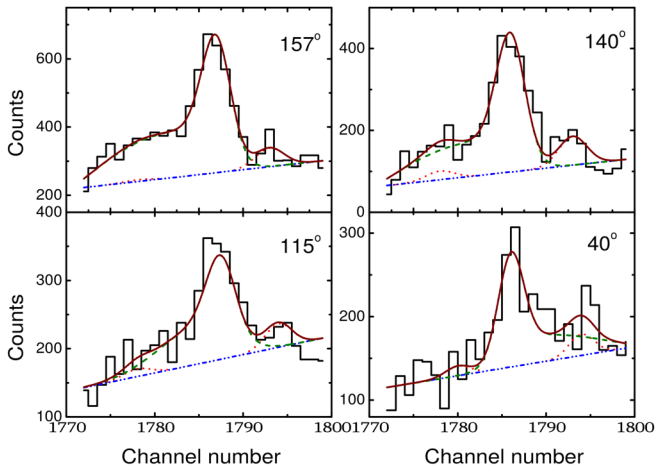

FIG. 6. The lineshape fits of 1787 keV γ rays at different angles. The blue line is the background, the red lines are the extra stopped peaks present in the fitted area, the green line is the lineshape fit for the attenuated Doppler shift and the brown line is the total fit of the spectrum.

40°. The fitted spectra are illustrated in Fig. 6. The details of the procedure used can be found in Refs. [31,32], however, for the ready reference a brief fitting procedure is given below.

1. Stopping powers: These are default defined in the DECHIST program via (i) Ward's effective charge [33], (ii) Ziegler's heavy-ion stopping powers [34], or (iii) shell-corrected Northcliffe and Schilling stopping powers [35]. But we have used updated stopping powers from newer version of the software SRIM [30], which are considered more reliable and are updated with the latest data of energy loss of atomic beams in the stopping media. These stopping powers are used to simulate the velocity (β) evolution of a given number of recoiling nuclei in the target and the backing media (in our case target acts as the backing stopping media also) using Monte Carlo techniques.
2. Cross-section dependence: For thin targets, the production cross section of recoiling nuclei can be considered constant with respect to the target thickness, because the beam energy loss within the thin target is negligible. However, in case of thick targets, the beam energy loss in the target in significant and, hence, the production cross section of recoiling nuclei cannot be considered constant anymore. This cross-section dependence is also considered in the DECHIST program itself, taken from the statistical model code PACE4 [36].

After all above considerations, for a history of 50 000 events, a 0.002 ps time step has been chosen for the simulation. The velocity profiles of the residual nuclei for detectors at 157°, 140°, 115°, and 40° have been calculated individually using the HISTAVER subprogram [28]. Furthermore, the expected Doppler shapes of a γ-ray energy at every angle has been calculated using the program LINESHAPE. The output of the LINESHAPE program is further matched with the actual corresponding experimental spectrum with a least-square fitting in order to extract the level lifetime τ. Here, for experimental spectra, we have made matrices with detectors at different angles: 157° vs 90°, 140° vs 90°, 115° vs 90°, 40° vs 90°; but the data were scarce to see shapes in γ lines so we have also made 157° vs rest, 140° vs rest, 115° vs rest, and 40° vs rest. Finally, these matrices were used for lineshape analysis. It is known that the spectra used for lifetime estimation in the DSAM are preferably generated from gating on the transitions above the transition of interest. This Gating on transition above (GTA) technique is typically plagued with insufficient statistics, for reliable fitting, in the peak of interest and the same has occurred in the present case. Alternatively, the analysis was carried out using spectra generated with gating on transition below (GTB) the transition of interest, wherein 1039 keV was used as the gating transition. The lifetime obtained from GTB, owing to the inherent uncertainty on the associated side feeding, is an upper limit on the result. In the present case, it came out to be $\leqslant$0.28 ps for the 2826 keV 3^- level in the ^{66}Zn nucleus. This is in reasonable overlap with the earlier known value of 0.26(1) ps reported from a Coulomb excitation measurement [14].

With this value of the measured lifetime, $\tau \leqslant 0.28$ ps; the calculated reduced transition probability is $B(E1) \geqslant 3.74 \times 10^{-4}$ W.u. for the 2826 keV level. It is enhanced by an order of two over the single-particle excitation, thus indicating the presence of collectivity. Enhancements in $B(E1)$ values in the similar range are reported in the $A \approx 220$ [37] and $A \approx 140$ [38] mass regions and these are understood in terms of octupole collectivity. The regions of the nuclei with strong octupole correlations correspond to particle numbers near 34 ($g_{9/2} \leftrightarrow p_{3/2}$ coupling), 56 ($h_{11/2} \leftrightarrow d_{5/2}$ coupling), 88 ($i_{13/2} \leftrightarrow f_{7/2}$ coupling), and 134 ($j_{15/2} \leftrightarrow g_{9/2}$ coupling) [3–5]. This nucleus ^{66}Zn with $Z = 30$ and $N = 36$ possesses $\Delta l = 3$ coupling for both the protons and the neutrons between $p_{3/2} \leftrightarrow g_{9/2}$; therefore, this large value of $B(E1)$ is indicative of the presence of octupole collectivity.

The behavior of the ratio of rotational frequency $\omega_{\rm rot}(\pi = -)/\omega_{\rm rot}(\pi = +)$ versus spin (I) of the discussed nucleus is shown in Fig. 7. This ratio is calculated as

$$\frac{\omega_{\rm rot}(\pi = -)}{\omega_{\rm rot}(\pi = +)} = 2\frac{E(I+1)^- - E(I-1)^-}{E(I+2)^+ - E(I-2)^+}, \tag{4}$$

which should be equal to unity for the perfectly reflection-asymmetric nuclei and should be equal to $[4(I-3)-2]/(4I-2)$ for the rotation of an aligned phonon. For ^{66}Zn, it is in-between the permanent octupole deformed and the octupole vibration at different spin levels.

To further support the involvement of octupole correlations in this nucleus, we calculated and plotted the $B(E1)/B(E2)$ ratio with spin, see Fig. 8. This ratio is calculated as

$$\left.\frac{BE(1)}{BE(2)}\right|_{atI} = 7.705 \times 10^{-7}\frac{(E_\gamma(E2))^5_{I\to I-2}}{(E_\gamma(E1))^3_{I\to I-1}}\frac{\mathrm{Int}(E1)}{\mathrm{Int}(E2)}\ \mathrm{fm}^{-2}, \tag{5}$$

where E_γ $(E1)$ and E_γ $(E2)$ are the energies of γ rays emitted from the same level in MeV, with multipolarity $E1$ and $E2$, respectively. Similarly, Int$(E1)$ and Int$(E2)$ are the intensities of the respective γ rays. Figure 8 shows clearly that the ratio is

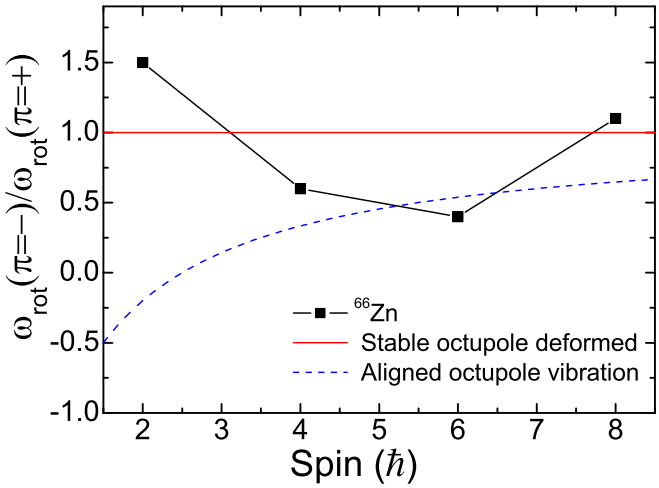

FIG. 7. Plot of $\omega_{\rm rot}(\pi = -)/\omega_{\rm rot}(\pi = +)$ versus spin for ^{66}Zn nuclei. This ratio should be equal to unity for the rotating rigidly reflection-asymmetric systems. The dashed blue line shows how it varies in the case of an aligned octupole phonon.

between 10^0 and $10^1 \times 10^{-6}$ fm^{-2}, which is an indication of the presence of the octupole collectivity in this nucleus. This value is in a similar range as for Ra–Th isotopes which are considered to be octupole deformed.

Furthermore, the level energies of the 2^+, 4^+, and 3^- states in the ^{62}Zn, ^{64}Zn, ^{66}Zn, ^{68}Zn, and ^{70}Zn isotopes are shown in Fig. 9. In these isotopic nuclei, the 3^- state is the lowest negative-parity state, the level energy of the 3^- state is decreasing as we add neutron pairs to ^{62}Zn and it reaches its lowest at ^{66}Zn and ^{68}Zn and come very close to the energy of the 4^+ level; this gap further increases for ^{70}Zn. This lowering of energy of the 3^- state indicates the increase in octupole correlations in the resulting nucleus; in other words, ^{66}Zn

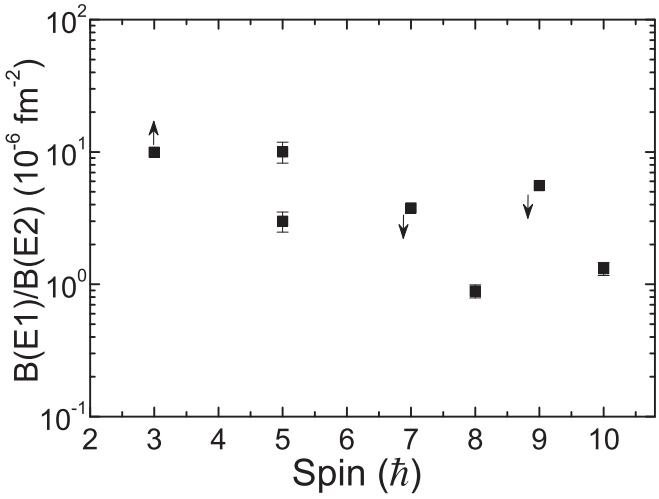

FIG. 8. The $B(E1)/B(E2)$ ratio of the yrast band at different spin levels of the yrast positive band states and the lowest negative-parity states. One data point (higher value) in the graph at the spin $5\hbar$ is the ratio of $B(E1)$ $(5^- \rightarrow 4_2^+)$ to $B(E2)$ $(5^- \rightarrow 3^-)$. The arrows $\uparrow$ and $\downarrow$ show the lower limit and the higher limit of the quantity, respectively.

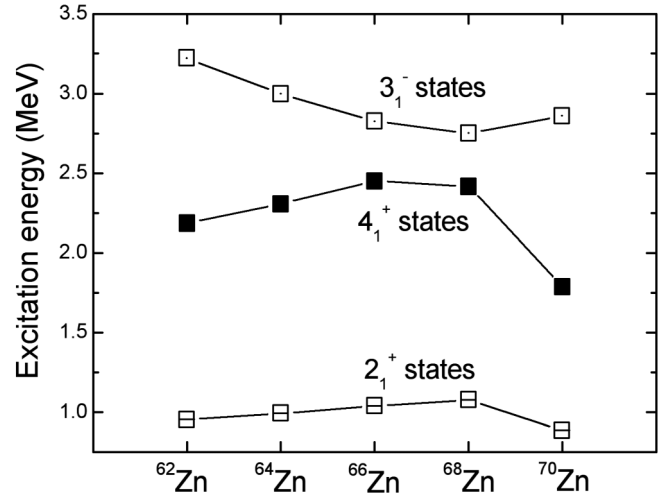

FIG. 9. The energy trend of the 2^+, 4^+, and 3^- states in the Zn isotopes.

and ^{68}Zn have the largest octupole collectivity in the isotopic chain. The next section deals with the theoretical calculations done to interpret in detail the experimental results obtained.

IV. DISCUSSION

The proposed partial level scheme of ^{66}Zn as shown in Fig. 5 shows the complex structure. In this section we discuss the observed level structure in the framework of the shell-model and TRS calculations.

A. Shell-model calculations

To understand the experimental findings of the energy levels microscopically, shell-model calculations were performed with a model space basis restricted to the $0f_{5/2}$, $1p_{3/2}$, $1p_{1/2}$, and $0g_{9/2}$ orbitals, which is known as the $jj44pn$ model space, using the NuShellX@MSU program [39]. No other restrictions were applied to the calculations. In this calculation, we used the $jj44bpn$ interaction, which has been successfully tested and used in this mass region [40,41]. The model assumes a closed ^{56}Ni core and does not allow core breaking. As the model space includes fpg orbitals, the calculations produced both positive- and negative-parity states. For ^{66}Zn, the fpg-shell model space has eight valence neutrons and two valence proton in the four active orbitals. The results of this calculation are compared with the experimental levels in Fig. 10. The yrast positive-parity states are reproduced well at low spins by the shell-model calculations; but as the spin increases, there is a gradual increase in deviation between the shell-model predicted and the experimental energy levels throughout the band structure, which indicates the development of collectivity along the positive-parity band. But there is mismatch in negative-parity experimental states above the 3^- spin level with the calculations, indicative of the presence of other anharmonicities in these states, which need to be included in the calculations to completely describe these states. Furthermore, the average particle occupancies of positive- and negative-parity levels and their respective con-

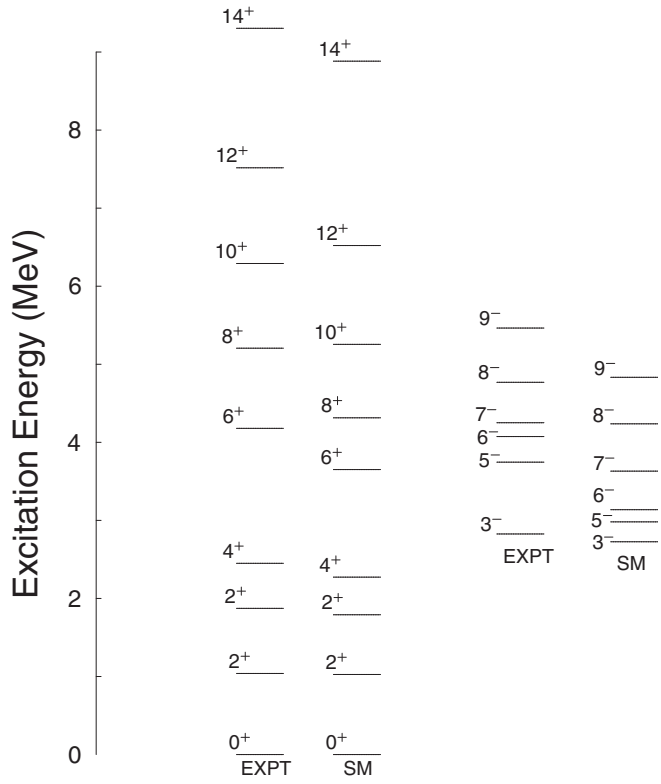

FIG. 10. Comparison of the energy levels of ^{66}Zn observed in the present data (denoted by EXPT) with the shell-model calculations using the *jj*44*bpn* [40] effective interaction (denoted SM) for the yrast positive-parity states and the lowest-energy negative-parity states.

figurations are listed in Tables II and III, respectively. From Table II, which accounts for occupancies of positive-parity states, it can be concluded that the contribution of the $\nu g_{9/2}$ orbital suddenly increases at the 8^+ level and is maximal at the same level. This shows the movement of a neutron pair from the lower f or p orbitals to the intruder g orbital. It is also

TABLE II. Average particle occupancies of the positive-parity states in ^{66}Zn from the shell-model calculations.

J^π	E_{expt} (keV)	E_{SM} (keV)	Particle	$0f_{5/2}$	$1p_{3/2}$	$1p_{1/2}$	$0g_{9/2}$
0^+	0	0	p	0.46	1.07	0.29	0.18
			n	3.09	2.89	0.78	1.24
2^+	1039	1026	p	0.50	0.99	0.37	0.14
			n	3.08	2.88	0.77	1.27
2_1^+	1873	1791	p	0.42	1.09	0.35	0.15
			n	3.04	2.92	0.98	1.07
4^+	2450	2273	p	0.83	0.80	0.28	0.09
			n	3.06	2.69	0.71	1.54
6^+	4179	3137	p	0.55	0.91	0.41	0.13
			n	3.11	3.04	0.55	1.30
8^+	5206	4314	p	0.73	0.73	0.46	0.08
			n	2.90	2.44	0.52	2.14
10^+	6292	5255	p	0.76	0.71	0.46	0.07
			n	2.87	2.48	0.52	2.13

TABLE III. Average particle occupancies of the negative-parity states in ^{66}Zn from the shell model calculations.

J^π	E_{expt} (keV)	E_{SM} (keV)	Particle	$0f_{5/2}$	$1p_{3/2}$	$1p_{1/2}$	$0g_{9/2}$
3^-	2826	2726	p	0.45	1.00	0.24	0.31
			n	3.28	2.47	0.80	1.44
1_2^-	3381	3480	p	0.67	0.82	0.38	0.13
			n	3.42	2.58	0.62	1.37
5^-	3746	2981	p	0.54	0.91	0.43	0.12
			n	3.13	2.93	0.60	1.34
6^-	4075	3137	p	0.55	0.91	0.41	0.13
			n	3.11	3.04	0.55	1.30
7^-	4251	3631	p	0.56	0.90	0.43	0.11
			n	2.97	3.03	0.62	1.37
9^-	5464	4833	p	0.73	0.82	0.36	0.08
			n	2.98	3.02	0.62	1.38

interpreted that, with increasing spin, the nucleus is becoming more deformed as the $\nu g_{9/2}$ orbital has shape-driving effects. For the negative-parity states, the proton occupancy for the 3^- state has the highest contribution of $\pi g_{9/2}$ orbitals in comparison to the other negative-parity states, which indicates that it is more deformed.

B. Total Routhian surface calculations

The microscopic structure of nuclei in the mass region $A \approx 60$–80 is primarily determined by $1f_{5/2}$, $2p_{3/2}$, $2p_{1/2}$, and $1g_{9/2}$ neutron and proton orbitals, as discussed in the above section. Although the single-particle level density in the $A \approx 60$–80 nuclei is comparatively lower than the other higher-mass regions, the shell structure effects manifest themselves in a dramatic way here. In particular, they give rise to strong shape variations as a function of both particle number and spin and thus lead to pronounced shape coexistence effects. The ^{66}Zn nucleus can be one of the good test cases in the region $A \approx 60$–80, in which the nucleus can exist on the onset of the shape transition. It is between the pure spherical and rotor limits. The nearby ^{64}Zn nucleus is claimed to exhibit $E(5)$-type structure [2] and the ^{66}Ni nucleus shows shape isomerism [1]. In the ^{66}Zn nucleus, with increasing spin, both the neutrons and the protons can occupy $1g_{9/2}$ orbitals (high j), which enhances the probability of existence of different nuclear shapes because this orbital has shape-driving effects. To see this effect, the aligned angular momentum i_x for the ground-state positive-parity band of the ^{66}Zn and ^{68}Ge nuclei is shown in Fig. 11. It is determined by subtracting the spin of a reference rotor from the angular-momentum projection along the axis of rotation, I_x.

$$i_x = I_x - I_{\text{ref}} \tag{6}$$

where

$$I_x = \sqrt{I(I+1)^2 - K^2} \tag{7}$$

and

$$I_{\text{ref}} = (J_0 + J_1\omega^2)\omega, \tag{8}$$

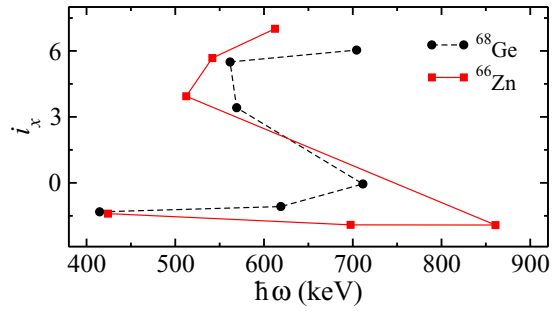

FIG. 11. Experimental alignments of the yrast positive-parity band as a function of rotational frequency in ^{66}Zn and ^{68}Ge. Harris parameters used for the calculation are $J_0 = 6.0\hbar^2$ MeV^{-1} and $J_1 = 3.5\hbar^4$ MeV^{-3} [42].

where J_0 and J_1 are Harris parameters, I is the total angular momentum, and K is the projection of I along the symmetry axis. In the ^{68}Ge nucleus, the levels up to $I = 6$ have been compared with excited variation after mean-field projection in realistic model space (EXVAM) calculations and interpreted as almost pure oblate states [43]. However, above $I = 8\hbar$, one neutron aligned band is consistent with the prediction and the configuration is calculated to have a prolate shape after band crossing [44]. A similar kind of variation in the structure is seen in the present ^{66}Zn nucleus, which may indicate a similar shape of this nucleus, i.e., it implies a neutron alignment band as the possible reason for backbending in ^{66}Zn above $I = 8\hbar$. Figure 11 shows that there is a gain in alignment of $\approx 8\hbar$ at the rotational frequency of $\approx$0.6 MeV for the ^{66}Zn nucleus. To understand the observed alignment, we calculated and plotted quasiparticle Routhians for both the protons and neutrons in Fig. 12, which indicates the feasibility of neutron alignment at $\approx$0.55 MeV, as discussed in detail later in the text.

To study the shape of ^{66}Zn nucleus theoretically, the total Routhian surfaces (TRSs) are calculated at different rotational frequencies ω. The total Routhian contains the macroscopic liquid drop energy of the nucleus, the shell correction, and the pairing energy. The single-particle energies are obtained from a Woods-Saxon potential [45]. The Routhian is minimized with respect to the deformation parameters β_2, β_4, and γ. The TRS calculations have been performed for the yrast band, with positive parity and positive ($\alpha = 0$) signature in accordance with the experimental observations. The calculated contour plots for the ground-state band are shown in Figs. 13 and 14.

As can be seen in Fig. 13, the predicted shape at low frequency ($\hbar\omega = 0.15$ MeV) is a shallow minimum with more bend towards an oblate collective shape with $\beta_2 = 0.22$. It is in good agreement with the earlier theoretical calculation by Moller *et al.* [46]. However, in Fig. 14, at $\hbar\omega = 0.35$ MeV, the minimum is clear and is at $\beta_2 = 0.25$, $\gamma = -50^\circ$ predicts that the nucleus is of triaxial shape at this frequency. As we further increase the rotational frequency ($\hbar\omega = 0.65$ MeV), the system goes into a nonminimum state, which clearly reflects that we cannot rotate the nucleus with the same configuration and the possibility of neutron-pair breakup arises, which is also visible by the alignment plot in Fig. 11. There is a gain in alignment of $\approx 8\hbar$ at 0.6 MeV frequency, which can be understood as an additional pair of particles, in this case neutrons, moved in the $\nu g_{9/2}$ orbitals, thereby inducing the change in the shape of the nucleus. Furthermore, theoretically calculated neutron and proton single-quasiparticle Routhians

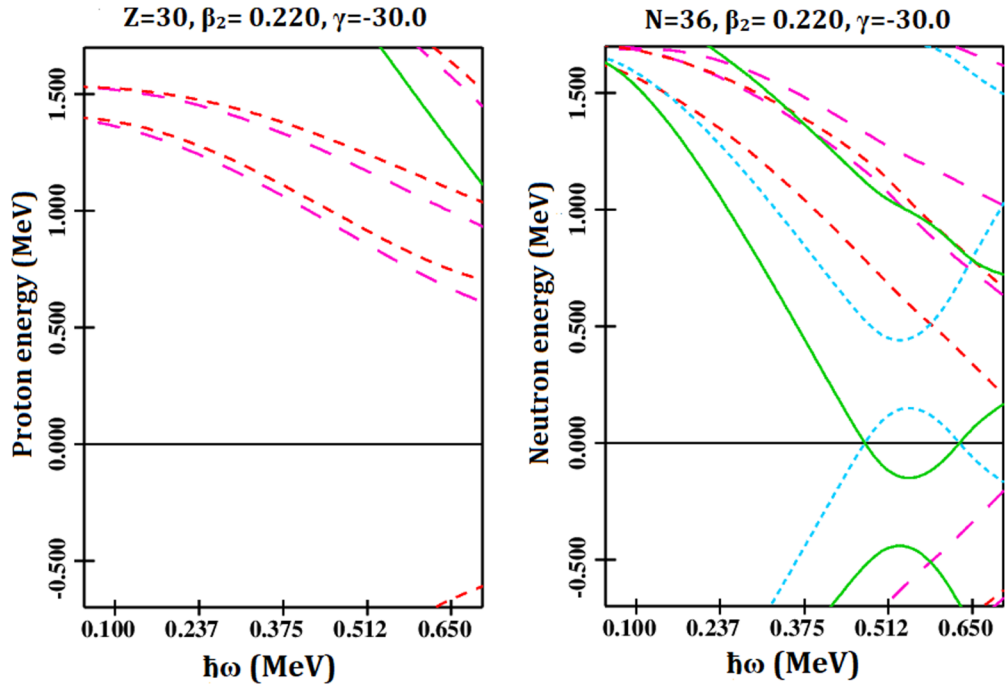

FIG. 12. Calculated quasiparticle energies for proton and neutron for ^{66}Zn at deformation $\beta_2 = 0.22$, $\gamma = 0^\circ$. The green lines denote the positive parity, positive signature; the blue lines denote the positive parity, negative signature; the red lines denote the negative parity, positive signature; and the magenta lines denote the negative parity, negative signature.

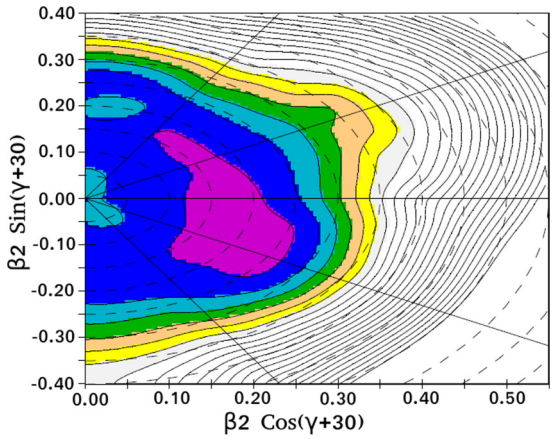

FIG. 13. TRS plot for zero quasiparticle configuration for ^{66}Zn at $\hbar\omega = 0.15$ MeV. The energy separation between the two consecutive surface contours is 250 keV.

at deformation values of $\beta_2 = 0.22$ and $\gamma = 0^\circ$ are shown in Fig. 12. It is evident from the figure that two-neutron alignment occurs at ≈0.6 MeV. This band crossing of $\nu g_{9/2}$ orbitals at ≈0.6 MeV, means that a neutron pair is moved to the $\nu g_{9/2}$ orbital above this energy; while there is no such crossing for the protons in this energy region. So the nucleus is oblate at low spin and triaxial at medium spin and further rotation leads to the breakup of a neutron pair.

V. CONCLUSIONS

Excited states of the ^{66}Zn nucleus have been investigated by using the reaction ^{56}Fe(^{12}C, $2p$)^{66}Zn at an incident-beam energy of ≈62 MeV using the Indian National Gamma Array (INGA). The level scheme of ^{66}Zn has been extended both for the low- and the high-spin states with the observation of twenty-one (seventeen are confirmed and four are tentative) new γ-ray transitions. The directional correlation measurements have been performed to assign the spin for most of the levels decaying via reported high-intensity γ-ray transitions. The polarization measurements of the intense γ rays

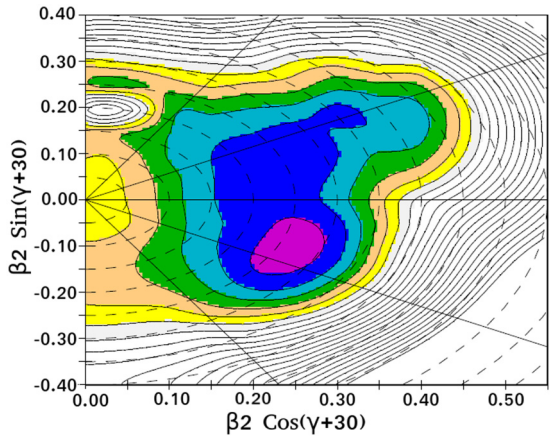

FIG. 14. Same as Fig. 13 but at $\hbar\omega = 0.35$ MeV.

have been done for this nucleus, which enables us to assign new and prove older assigned parities for the nuclear states. The microscopic origin of the investigated level structures is discussed in the context of large shell-model calculations in the fpg model space using the $jj44bpn$ effective interaction. Shell-model calculations show the increase of involvement of $\nu g_{9/2}$ and $\pi g_{9/2}$ orbitals with increasing spin, which is indicative of nuclear-shape changes with increasing spin. The lifetime of the 3^- state at 2826 keV is determined by DSAM analysis of the 1787 keV γ ray, which satisfactorily matches with earlier reported values. The calculated $B(E1)$ value from the lifetime of the 3^- state is 3.74×10^{-4} W.u., which is two orders of magnitude higher than the normal single-particle state transition; a similar enhancement in the $B(E1)$ values is also been seen for octupole-deformed Ra, Th, and Ba isotopes and thus indicates the presence of octupole collectivity in the present nucleus ^{66}Zn. The yrast negative-parity states are connected with positive-parity yrast states with fast $E1$ transitions; the $\omega(-)/\omega(+)$ and $B(E1)/B(E2)$ plots for these states show the presence of octupole correlations in this nucleus. Furthermore, the total Routhian surface (TRS) calculations have also been carried out, which suggest oblate and triaxial deformation at low and medium spins and alignment of neutron pairs at further rotation for the yrast band. In comparison with the recent work by Rai *et al.* [15] on the same nucleus ^{66}Zn, a similar conclusion about the nuclear shape in the positive-parity yrast band has been made in the present study. While for negative-parity states, Ref. [15] concludes on the basis of TRS calculations that the nucleus evolves from moderately deformed triaxial at low spins to well-deformed prolate at high spins; however, in the present study it is observed and concluded that the octupole correlations play an important role in the ^{66}Zn nucleus and that the nucleus is of octupole shape at low spins via measuring the electric-dipole transition probability from the $3^- \rightarrow 2^+$ state.

This study shows that the ^{66}Zn nucleus has large octupole correlations which are visible through its enhanced $B(E1)$ values. We suggest that future experimental efforts could be done to measure $B(E3)$ values of this nucleus. This whole region can be a matter of further investigation for octupole collectivity. Also, the ^{66}Zn nucleus is oblate shaped in the ground state, which changes its shape upon rotation with the involvement of $\nu g_{9/2}$ orbitals in its microscopic configuration and alignment of a neutron pair. Further, many new non-yrast bands observed in this nucleus need further experimental and theoretical study to gain knowledge about the microscopic and macroscopic structure involved.

ACKNOWLEDGMENTS

The authors gratefully acknowledge the support provided by the staff of the TIFR-BARC pelletron facility for providing a stable beam, the target laboratory staff at IUAC, and the INGA Collaboration. The Director of the IUAC is highly acknowledged for the support and encouragement throughout this research. We acknowledge the Department of Science and Technology, Government of India, for providing funds for the INGA project (No. IR/S2/PF-03/2003-I).

[1] S. Leoni *et al.*, Phys. Rev. Lett. **118**, 162502 (2017).
[2] C. Mihai, N. V. Zamfir *et al.*, Phys. Rev. C **75**, 044302 (2007).
[3] I. Ahmad and P. A. Butler, Annu. Rev. Nucl. Part. Sci. **43**, 71 (1993).
[4] P. A. Butler and W. Nazarewicz, Rev. Mod. Phys. **68**, 349 (1996).
[5] P. A. Butler, J. Phys. G **43**, 073002 (2016).
[6] L. Cleemann *et al.*, Nucl. Phys. A **386**, 367 (1982).
[7] G. F. Neal *et al.*, Nucl. Phys. A **280**, 161 (1977).
[8] J. F. Bruandet, M. Agard, A. Giorni, J. P. Longuequeue, C. Morand, and T. U. Chan, Phys. Rev. C **12**, 1739 (1975).
[9] M. Calderbank, E. J. Burge, and D. A. Smith, Phys. Lett. B **25**, 201 (1967).
[10] K. Yagi and Y. Sazi, Nucl. Phys. A **132**, 690 (1969).
[11] D. H. Youngblood, Nucl. Phys. A **183**, 197 (1972).
[12] M. Ivascu, Nucl. Phys. A **218**, 104 (1974).
[13] R. N. Horoshko, H. L. Scott, and D. M. Van Patter, Phys. Rev. **185**, 1470 (1969).
[14] J. Leske, K.-H. Speidel, S. Schielke, J. Gerber, P. Maier-Komor, T. Engeland, and M. Hjorth-Jensen, Phys. Rev. C **73**, 064305 (2006).
[15] S. Rai *et al.*, Phys. Rev. C **102**, 064313 (2020).
[16] R. Palit, S. Saha, J. Sethi, T. Trivedi, B. S. Naidu, P. B. Chavan, R. Donthi, and S. Jadhav, J. Phys.: Conf. Ser. **420**, 012159 (2013).
[17] R. Palit, S. Saha, J. Sethi, T. Trivedi, S. Sharma, B. S. Naidu, S. Jadhav, R. Donthi, P. B. Chavan, H. Tan *et al.*, Nucl. Instrum. Methods Phys. Res., Sect. A **680**, 90 (2012).
[18] H. Tan *et al.*, *IEEE Nuclear Science Symposium Conference Record Washington, DC* (IEEE, Piscataway, NJ, 2008), p. 3196.
[19] D. C. Radford, Nucl. Instrum. Methods Phys. Res., Sect. A **361**, 297 (1995).
[20] D. C. Radford, Nucl. Instrum. Methods Phys. Res., Sect. A **361**, 306 (1995).
[21] B. P. A. Kumar, E. T. Subramaniam, K. M. Jayan, S. Mukherjee, and R. K. Bhowmik, CANDLE-Collection and Analysis of Nuclear Data using Linux nEtwork, Proc. DAE Sym **44B**, 390 (2001).
[22] A. Krämer-Flecken, T. Morek, R. M. Lieder, W. Gast, G. Hebbinghaus, H. M. Jäger, and W. Urban, Nucl. Instrum. Methods Phys. Res., Sect. A **275**, 333 (1989).
[23] M. K. Kabadiyski, K. P. Lieb, and D. Rudolph, Nucl. Phys. A **563**, 301 (1993).
[24] G. Duchene *et al.*, Nucl. Instrum. Methods Phys. Res., Sect. A **432**, 90 (1999).
[25] K. Starosta *et al.*, Nucl. Instrum. Methods Phys. Res., Sect. A **423**, 16 (1999).
[26] O. Klein and Y. Z. Nishina, Z. Phys. **52**, 853 (1929).
[27] S. Das *et al.*, Nucl. Instrum. Methods Phys. Res., Sect. A **841**, 17 (2017).
[28] J. C. Wells and N. R. Johnson, LINESHAPE: A computer program for doppler broadened lineshape analysis, Report No. ORNL-6689, 44 (1991).
[29] N. R. Johnson, J. C. Wells, Y. Akovali, C. Baktash, R. Bengtsson, M. J. Brinkman, D. M. Cullen, C. J. Gross, H.-Q. Jin, I.-Y. Lee, A. O. Macchiavelli, F. K. McGowan, W. T. Milner, and C.-H. Yu, Phys. Rev. C **55**, 652 (1997).
[30] www.srim.org.
[31] R. Bhattacharjee *et al.*, Phys. Rev. C **90**, 044319 (2014).
[32] S. Rajbanshi *et al.*, Phys. Lett. B **782**, 143 (2018).
[33] D. Ward, J. S. Forster, H. R. Andrews, I. V. Mitchell, G. C. Ball, W. G. Davies, and G. J. Costa, AECL Report No. 5313 (1976), https://inis.iaea.org/collection/NCLCollectionStore/_Public/07/258/7258444.pdf.
[34] J. F. Ziegler, *The Stopping and Ranges of Ions in Matter* (Pergamon, Oxford, 1980).
[35] L. C. Northcliffe and R. F. Schilling, At. Data Nucl. Data Tables **7**, 233 (1970).
[36] http://lise.nscl.msu.edu/pace4.html.
[37] L. P. Gaffney, P. A. Butler *et al.*, Nature (London) **497**, 199 (2013).
[38] B. Bucher *et al.*, Phys. Rev. Lett. **116**, 112503 (2016).
[39] B. A. Brown and W. D. M. Rae, "Nushellx@MSU" MSU-NSCL Report 524:1-29 (2007).
[40] C. J. Chiara, D. Weisshaar, R. V. F. Janssens, Y. Tsunoda, T. Otsuka, J. L. Harker, W. B. Walters, F. Recchia, M. Albers, M. Alcorta *et al.*, Phys. Rev. C **91**, 044309 (2015).
[41] A. F. Lisetskiy, B. A. Brown, M. Horoi, and H. Grawe, Phys. Rev. C **70**, 044314 (2004).
[42] B. Mukherjee, S. Muralithar, R. P. Singh, R. Kumar, K. Rani, R. K. Bhowmik, and S. C. Pancholi, Phys. Rev. C **64**, 024304 (2001).
[43] A. Petrovici, K. W. Schmid, F. Grummer, and A. Faessler, Nucl. Phys. A **517**, 108 (1990).
[44] U. Hermkens, F. Becker, J. Eberth, S. Freund, T. Mylaes, S. Skoda, W. Tiechert, and A. V. D. Werth, Z. Phys. A: Hadrons Nucl. **343**, 371 (1992).
[45] W. Nazarewicz, J. Dudek, R. Bengtsson, T. Bengtsson, and I. Ragnarsson, Nucl. Phys. A **435**, 397 (1985).
[46] P. Moller *et al.*, At. Data Nucl. Data Tables **59**, 185 (1995).